Photoluminescence Tuning in Novel Bi^{3+}/Mn^{4+} Co-doped La_2ATiO_6:(A = Mg, Zn) Double Perovskite Structure: Phase Transition and Energy Transfer

Gongcheng Xing,[†] Yuxin Feng,[†] Min Pan,[†] Yi Wei,[†] Guogang Li,[†,*] Peipei Dang,[‡] Sisi Liang,[‡] Maxim S. Molokeev,[§, Δ, #] Ziyong Cheng,[‡] Jun Lin[‡,*]

[†]Engineering Research Center of Nano-Geomaterials of Ministry of Education, Faculty of Materials Science and Chemistry, China University of Geosciences, 388 Lumo Road, Wuhan 430074, P. R. China

[‡]State Key Laboratory of Rare Earth Resource Utilization, Changchun Institute of Applied Chemistry, Chinese Academy of Sciences, Changchun 130022, P. R. China

[§]Laboratory of Crystal Physics, Kirensky Institute of Physics, SB RAS, Krasnoyarsk 660036, Russia

[Δ]Department of Physics, Far Eastern State Transport University, Khabarovsk, 680021 Russia

[#]Siberian Federal University, Krasnoyarsk, 660041, Russia

[є]School of Applied Physics and Materials, Wuyi University, Jiangmen, Guangdong, 529020, P. R. China

KEYWORDS: Mn^{4+}; double perovskite structure; phase transition; energy transfer; red-emitting improvement.

Supporting Information

ABSTRACT: To achieve warm white light of phosphor-converted white light emitting diodes (pc-WLEDs), red-emitting phosphors are indispensable to improve lighting quality. In this work, we develop red-emitting double perovskite phosphors La_2ATiO_6:Bi^{3+}, Mn^{4+} (A = Mg, Zn) (LAT: Bi^{3+}, Mn^{4+}). Through designing Mg^{2+}/Zn^{2+} cation substitution and $Bi^{3+}\rightarrow Mn^{4+}$ energy transfer strategies, the photoluminescence properties of Bi^{3+} and Mn^{4+} emission are remarkably tuned and optimized. Rietveld refinement results demonstrate that La_2MgTiO_6:Bi^{3+}, Mn^{4+} (LMT: Bi^{3+}, Mn^{4+}) belongs to orthorhombic structure (*Pbnm*) with one Ti/Mg site, while La_2ZnTiO_6: Bi^{3+}, Mn^{4+} (LZT: Bi^{3+}, Mn^{4+}) crystallizes in monoclinic structure ($P2_1/n$) with two Ti1/Zn1 and Ti2/Zn2 sites. Notably, the phase transition appears in $La_2Mg_{(1-w)}Zn_wTiO_6$:Bi^{3+}, Mn^{4+} ($0 \le w \le 1$) ($LM_{(1-w)}Z_wT$:Bi^{3+}, Mn^{4+}) solid solution, resulting in a lower local structure symmetry of [LaO_{12}] polyhedron and crystal field environment, which is the proposed reason for red-shift emission adjustment of Bi^{3+} ions. Due to the energy transfer of $Bi^{3+}\rightarrow Mn^{4+}$ in LAT, red emission of Mn^{4+} ions could be dramatically enhanced. The energy transfer efficiency of LAT: Bi^{3+}, Mn^{4+} eventually reaches more than 90%. Moreover, the thermal stability is improved by Mg^{2+}/Zn^{2+} cation substitution and $Bi^{3+}\rightarrow Mn^{4+}$ energy transfer strategies for LAT:Bi^{3+}, Mn^{4+} and $LM_{(1-w)}Z_wT$:Bi^{3+}, Mn^{4+} respectively. The performance of the fabricated pc-WLEDs devices indicates that LAT:Bi^{3+}, Mn^{4+} could be a promising red phosphor for near ultraviolet (n-UV) based warm white light pc-WLEDs. The influence of local structure symmetry and $Bi^{3+}\rightarrow Mn^{4+}$ energy transfer on luminescence tuning and improvement are efficient strategy to exploit novel red-emitting phosphor and could offer a guidance to develop new phosphors system.

■ INTRODUCTION

Nowadays, phosphor-converted white light emitting diodes (pc-WLEDs) have widely been used in lighting and display area due to high efficiency, long lifetime, excellent energy conservation, environmental friendliness and so on.[1-6] The commercially available pc-WLEDs devices infer the combination of blue InGaN LED chip and yellow YAG:Ce^{3+} phosphor. Whereas, owe to the lack of enough red component in the emission spectra, the fabricated pc-WLEDs produces cold white light with high CCT (≥ 7750K) and low CRI (Ra = 70–80), which easily makes people's eyes feel tired in a long-term use.[7-9] To overcome the above drawback, a burgeoning n-UV InGaN based pc-WLEDs chip by combining trichromatic phosphors enter people's field of vision.[10-12] Hence, red-emitting phosphors are necessary to improve lighting quality of pc-WLEDs. The usually red-emitting phosphors are Eu^{2+}-activated nitrides phosphors, such as $Sr_2Si_5N_8$:Eu^{2+} [13] and $CaSiAlN_3$:Eu^{2+}.[14] Although they exhibit highly efficient red emission, the harsh synthesis condition (high temperature and high pressure) brings expensive instrument cost and limits the extensive application in pc-WLEDs. Eu^{3+} always emits linear red emission due to the characteristic $4f$–$4f$ partial spin and forbidden transition. Since its absorption is very weak in n-UV and blue region, Eu^{3+} is hardly utilized in warm pc-WLEDs due to low luminescence efficiency.[15,16] Thus, exploiting novel red-emitting phosphor has been still a big challenge.

Recently, many researchers have pay attention to exploring non-rare earth ions activated red phosphors. Mn^{4+} mainly emits narrow-band red light in fluoride and oxide due to the typical $^2E_g\rightarrow{}^4A_{2g}$ transition. Mn^{4+}-activated fluoride phosphor

has been widely reported due to its superb red emission and high quantum yield. For instance, Zhu et al. reported a highly efficient micrometre-sized $K_2TiF_6:Mn^{4+}$ phosphor with the quantum yield even exceeding 98% by using a novel cation substitution strategy.[17] Fang et al. developed a series narrow-band red-emitting $Na_2(Si_xGe_{1-x})F_6:Mn^{4+}$ and $Na_2(Ge_yTi_{1-y})F_6:Mn^{4+}$ solid solutions with the luminous efficacy of the radiation value achieving 235 lm/W_{opt}.[18] Although Mn^{4+} doped fluoride phosphor matches well with n-UV or blue LED chip and exhibits excellent red-emitting properties, the abundant use of corrosive HF acid is dangerous and poisonous. Moreover, this phosphor always accompanies with serious chemical stability in air, which limits the large-scale application in WLEDs. For Mn^{4+}-doped oxide phosphors, it could effectively avoid the serious chemical stability and thus appeal many researchers' attention. However, the luminescence efficiency of Mn^{4+} ions in oxide host need be improved. To enhance the red emission of Mn^{4+} ions in oxide host, the design of appropriate energy transfer is an effective strategy. Bi^{3+} is a good activator, which could emit various light in the whole visible region decided by the crystal field environment of host lattice due to the naked 6*s* and 6*p* orbit.[19-21] Except for using as activator, Bi^{3+} could act as an excellent sensitizer,[22,23] for example, Dang et al. designed $Bi^{3+}\rightarrow Eu^{3+}$ energy transfer in $LiCa_3MgV_3O_{12}$ phosphor, achieving full color photoluminescence tuning and enhanced red emission of Eu^{3+}.[24] $Bi^{3+}\rightarrow Mn^{4+}$ energy transfers could also be realized to enhance the red emission intensity. For instance, Zhou et al. reported the energy transfer induced tunable dual emission of $Ca_3Al_4ZnO_{10}:Bi^{3+}$, Mn^{4+} phosphor, which is suitable to be applied in agricultural fields.[23] Li et al. developed Bi^{3+}, Mn^{4+} co-doped $Ca_{14}Al_{10}Zn_6O_{35}$ phosphors of which the internal quantum yields (IQYs) is as high as 98.1%.[25]

Generally, Mn^{4+} could generate luminescence only in octahedral coordination environment. Double-perovskite $A_2BB'O_6$ (A-site cation is typically alkali, alkali earth, or rare earth cation; B and B'-site cation is typical transition metal or a main group element) is a very suitable matrix for Mn^{4+} ions doping to generate red emission. It consists of three-dimensional network by alternating $[BO_6]$ and $[B'O_6]$ octahedra, and A atoms occupy into the interstitial space.[26] On account of the pseudo-cubic symmetry and the relative B-cation disorder in many double-perovskite compounds, Mn^{4+} emission position slightly changes among different matrix system such as $CaYSbO_6:Mn^{4+}$ (680 nm),[27] $Ba_2GdSbO_6:Mn^{4+}$ (687 nm),[28] $KMgLaTeO_6:Mn^{4+}$ (696 nm)[29] and $BaLaMgNbO_6:Mn^{4+}$ (700 nm).[30] Besides, some researchers have achieved luminescence tuning by cation substitution strategy, such as $(Ba,Sr)YSbO_6:Mn^{4+}$ phosphor (685 nm).[31] These works indicate that luminescence could be tuned and modified by local coordination environment variation in Mn^{4+}-activated double-perovskite $A_2BB'O_6$ phosphors. Takeda et al. reported $La_2MgTiO_6:Mn^{4+}$ and $La_2ZnTiO_6:Mn^{4+}$ red phosphors with the maximum emission at 710 nm.[32] However, the relationship between luminescence properties and crystal structure has not been clearly revealed. In this work, we successfully design $La_{2(1-u/x)}ATi_{(1-z/y)}O_6:u/xBi^{3+}$, $z/y\ Mn^{4+}$ (A = Mg^{2+}, Zn^{2+}; $0 \le u/x \le 0.03$, $0 \le z/y \le 0.01$) phosphors and $La_2Mg_{(1-w)}Zn_wTiO_6:0.005Bi^{3+}$, $0.002Mn^{4+}$ ($0 \le w \le 1$) solid solution. Through Mg^{2+}/Zn^{2+} cation substitution and $Bi^{3+}\rightarrow Mn^{4+}$ energy transfer strategies, the local symmetry and coordination environment surrounding Mn^{4+} are slightly changed, resulting in luminescence adjustment and enhancement. On basis of Rietveld refinements, when Zn^{2+} ions gradually substitute Mg^{2+} ions, phase transition will appear. Local structure symmetry variation reveals potential mechanism of luminescence adjustment. Simultaneously, thermal stability is evidently improved by Bi^{3+}/Mn^{4+} co-doping and Mg^{2+}/Zn^{2+} cation substitution strategies. The performance of pc-WLEDs also indicates that as-prepared phosphor could act as the potential red candidate for warm pc-WLEDs. Our work could offer a new insight on the effect of local structure symmetry and energy transfer from Bi^{3+} on Mn^{4+} luminescence, which could offer a guidance in designing novel Mn^{4+}-doped phosphors.

■ EXPERIMENTAL SECTION

Materials and Preparation. A series of $La_{2(1-u/x)}ATiO_6:u/xBi^{3+}$ (LAT:u/xBi^{3+}), $La_2ATi_{(1-z/y)}O_6:z/yMn^{4+}$ (LAT:z/yMn^{4+}), and $La_{2(1-u/x)}(Mg_{1-w}Zn_w)Ti_{(1-z/y)}O_6:u/xBi^{3+}$, z/yMn^{4+} (A = Mg, Zn; $u/x = 0-0.03$, $z/y = 0-0.01$, $w = 0, 0.25, 0.50, 0.75, 1.0$) compounds were prepared by a traditional high temperature solid-state reaction in air. For $La_{2(1-u/x)}ATi_{(1-z/y)}O_6:u/xBi^{3+}$, z/yMn^{4+} samples, they are abbreviated to be LMT:uBi^{3+}, zMn^{4+} for A = Mg, LZT:xBi^{3+}, yMn^{4+} for A = Zn, and L(M, Z)T:xBi^{3+}, yMn^{4+} for A = (Mg, Zn), respectively. In a typical preparation process, the raw materials were La_2O_3 (Aladdin), MgO (Aladdin), TiO_2 (Aladdin), ZnO (Aladdin), Bi_2O_3 (Aladdin) and $MnCO_3$ (Aladdin) with a purity of ≥ 99.99% without further processing. Stoichiometric raw materials were weighted and mixed together for sufficiently grinding 30 mins in an agate mortar with pestle, then the mixture was put into alumina crucibles and sintered in a tube furnace at 1400 °C for 10 h in air. After cooling down to room temperature naturally, the resulting phosphor powders were successfully achieved by again grinding.

pc-WLEDs Devices Fabrication. pc-WLEDs were fabricated by combining 420 nm InGaN chips and the mixture of representative LZT:$0.005Bi^{3+}$, $0.01Mn^{4+}$ phosphor and commercially available green $Ba_3Si_6O_{12}N_2:Eu^{2+}$ phosphor. The proper amounts of phosphors were added into the epoxy resins and mixed thoroughly for 20 min. The acquired mixture was coated on the surface of the 420 nm InGaN chips and dried at 120 °C to produce WLEDs. All measurements were carried out at 20 mA drive current.

Characterization. The X-ray diffraction (XRD) data for phase purity and structural detection of the as-prepared samples were obtained by using a D8 Focus diffractometer at as canning rate of 1° min^{-1} in the 2θ range from 10° to 120° with Nifiltered Cu Kα (λ = 1.540598 Å). The Rietveld profile refinements of structural models and texture analysis by the General Structure Analysis System (GSAS) software. The morphologies, energy-dispersive X-ray spectrum (EDS) and elemental mapping analysis of the samples were inspected using a field emission scanning electron microscope (FE-SEM, S−4800, Hitachi). The photoluminescence quantum yield (QY) was collected by an absolute PL quantum yield measurement system C9920-02 (Hamamatsu photonics K.K., Japan). The high-resolution transmission electron microscopy (HRTEM) were obtained with the use of FEI Tecnai G2 F20. The diffuse reflectance spectra (DRS) were recorded by UV−visible diffuse reflectance spectroscopy UV−2550PC (Shimadzu Corporation, Japan). The photoluminescence excitation (PLE) and emission (PL) spectra were measured by a fluorescence spectrometer (Fluoromax-4P, Horiba Jobin Yvon, New Jersey, U.S.A.) equipped with a 150 W xenon

lamp as the excitation source, and both excitation and emission spectra are set up to be 1.0 nm with the width of the monochromator slits adjusted to 1.0 nm. The lifetimes of as-prepared samples were detected by a Lecroy Wave Runner 6100 Digital Osilloscope (1 GHz) using a tunable laser (pulse width = 4 ns; gate = 50 ns) as the excitation (Contimuum Sunlite OPO). The thermal stabilities of luminescence properties were performed by Fluoromax-4P spectrometer connected heating equipment (TAP-02) and using a combined setup consisting of a Xe lamp, a Hamamatsu MPCD-7000 multichannel photodetector, and a computer-controlled heater. Commission Internationale de l'Eclairage chromaticity color coordinates, color rendering index (CRI), and corresponding color temperature (CCT) of WLEDs devices were measured by using an integrating sphere with an analyzer system (tarspec SSP6612).

■ RESULTS AND DISCUSSION

Effect of Phase Transition on Luminescence Properties

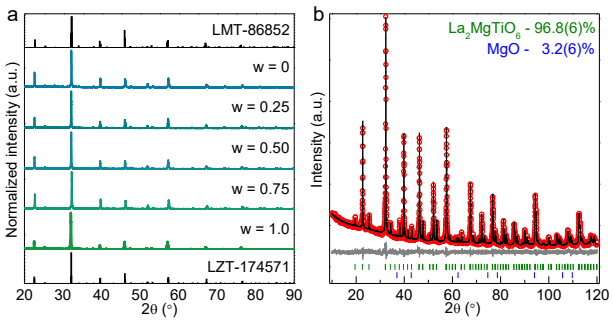

Figure 1. (a) XRD patterns of $LM_{(1-w)}Z_wT$:0.005Bi^{3+}, 0.002Mn^{4+} ($0 \le w \le 1$) samples and the standard La_2MgTiO_6 (ICSD No. 86852) and La_2ZnTiO_6 (ICSD No. 174571). (b) Rietveld refinement XRD data of the representative LMT:0.005Bi^{3+}, 0.002Mn^{4+} sample with the measured data (red circle), fitted data (black line), difference (grey line) and Bragg position (olive vertical bar). Blue vertical bar is the Bragg position of MgO impurity.

Powder X-ray diffraction (XRD) provides a direct evidence for the confirmation of phase purity and crystal structure of the as-prepared compounds. Figure 1a demonstrates the typical XRD patterns of $LM_{(1-w)}Z_wT$:0.005Bi^{3+}, 0.002Mn^{4+} ($0 \le w \le 1$). Obviously, the XRD patterns of $w = 0$ and $w = 1$ samples can be well assigned to the standard La_2MgTiO_6 (marked as LMT, ICSD No. 86852) and La_2ZnTiO_6 (marked as LZT, ICSD No. 174571) phases, respectively. As the Zn^{2+} substitution concentrations w increase, the XRD diffraction peaks of $LM_{(1-w)}Z_wT$:0.005Bi^{3+}, 0.002Mn^{4+} ($0 \le w \le 1$) samples exhibit a monotonous shift toward small-angle direction without any impurities, which is ascribed to the replacement of larger Zn^{2+} (r = 0.74 Å, CN = 6) for Mg^{2+} (r = 0.72 Å, CN = 6). This result implies the successful substitution of Zn^{2+} ions into the Mg^{2+} sites and the formation of solid solutions. To further investigate the crystal structure of solid solution, the XRD patterns of $LM_{(1-w)}Z_wT$:0.005Bi^{3+}, 0.002Mn^{4+} ($0 \le w \le 1$) with 2θ range from 10° to 120° were performed with Rietveld refinement. Almost all reflection peaks for $w = 0$ sample, besides small amounts of tiny peaks which belongs to MgO phase, are indexed by orthorhombic cell (*Pbnm*) with parameters close to La_2MgTiO_6 (double perovskite-type structure),[33,34] as shown in Figure 1b. Other XRD Rietveld refinement patterns for w = 0.25-1.0 samples are listed in Figure S1 (Supporting Information). When Zn^{2+} ions completely substitute Mg^{2+} ions ($w = 1$), its XRD pattern could be very well fitted by monoclinic cell ($P2_1/n$) with lattice parameters close to La_2ZnTiO_6.[35] Main parameters of processing and refinement of the $LM_{(1-w)}Z_wT$:0.005Bi^{3+},0.002Mn^{4+} samples is summarized in Table 1. Although, there exists minor peaks of $La_2Ti_2O_7$ phase ($Pna2_1$), refinements of all models are stable and give low R-factors (Table 1), confirming the formation of pure phases. What's more, due to equal charge valence (+3) and similar ions radius between La^{3+} (r = 1.36 Å, CN = 12) and Bi^{3+} (r = 1.17 Å, CN = 8). Bi^{3+} is suggested to occupy La^{3+} sites. Similarly, Mn^{4+} ions are suggested to occupy (Ti/Mg/Zn) site ($r[Mn^{4+}]$ = 0.53 Å, CN = 6; $r[Ti^{4+}]$ = 0.605 Å, CN = 6). However, the doped Bi^{3+} and Mn^{4+} contents are too small to obtain their trace in $LM_{(1-w)}Z_wT$ ($0 \le w \le 1$) by Rietveld refinement. Table S1 and Table S2 collect the coordinates of atoms and main bond lengths, respectively. Surprisingly, the XRD patterns of the samples with $w \ge 0.25$ reveal noticeable peak broadening and the full width at half maximum (fwhms) change at 2θ = 57.4º with a jump from $w = 0$ to $w = 0.25$, as presented in the Figure S2 (Supporting Information). This obvious jump between $w = 0$ and $w = 0.25$ can be associated with the phase transition from *Pbnm* to $P2_1/n$ phases. The cell parameters per Zn^{2+} concentration w (Figure 2) also show jump in the range of w = 0-0.25, further proving the existence of the phase transition *Pbnm* ↔ $P2_1/n$. According to the previous report, Aguadero et al.[35] proved that there are two Zn^{2+} sites in La_2ZnTiO_6, and Ti^{4+}/Zn^{2+} ions are intermixed in two sites. Meden et al.[33] also showed that Ti^{4+}/Mg^{2+} ions in La_2MgTiO_6 are also intermixed. In our case, the Mg^{2+} ions are replaced by Zn^{2+} ions, and thus we suggest Zn/Ti/Mg intermixing. The occupations occ(Zn), occ(Ti) and occ(Mg) are refined with linear restrictions, so that the resulting chemical formula stays similar to suggested one. All cell parameters increase with w increasing starting from $w = 0.25$, which is in a good agreement with bigger Zn^{2+} ion radius than Mg^{2+} ion radius (Figure 2). In addition, the average bond length d(Ti/Mg/Zn–O) increases with w increasing (Figure S3), and all these facts prove reliability of the suggested chemical formulas.

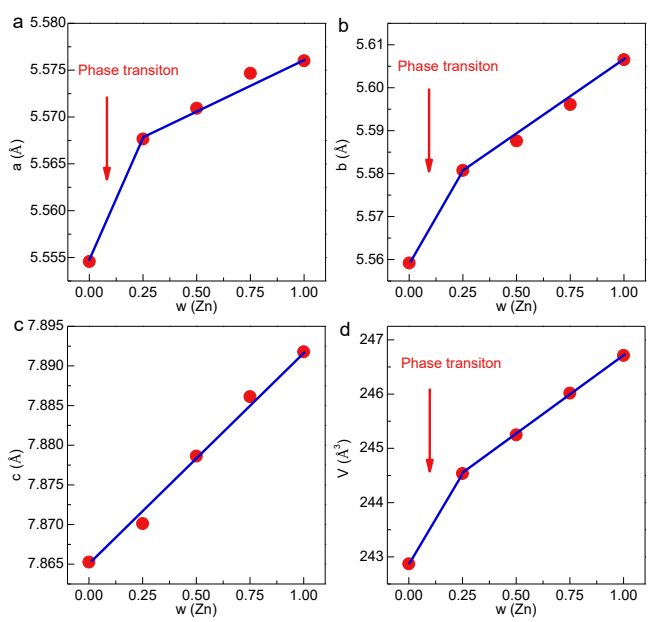

Figure 2. The cell parameters of $LM_{(1-w)}Z_wT$:0.005Bi^{3+}, 0.002Mn^{4+} ($0 \le w \le 1$) dependences per Zn^{2+} concentration (w): (a) a; (b) b; (c) c; (d) V. The red arrows represent the probable region of the phase transition between *Pbnm* and $P2_1/n$ phases.

Table 1. Main parameters of processing and refinement of the $LM_{(1-w)}Z_wT$:0.005Bi^{3+}, 0.002Mn^{4+} ($0 \le w \le 1$) samples

w	Phase	Weight (%)	Space group	Cell parameters (Å, Å^3)	R_p (%), χ^2	R_B (%)	Impurities
0	La_2MgTiO_6	96.8(6)	*Pbnm*	a = 5.5546(2) b = 5.5592(1) c = 7.8652(2) V = 242.87(1)	6.64, 5.09, 1.41	2.42	MgO
	MgO	3.2	*Fm*-3*m*	a = 4.2118(3) V = 74.724 (2)		0.72	
0.25	$La_2Mg_{0.75}Zn_{0.25}TiO_6$	94(2)	$P2_1/n$	a = 5.5692(2) b = 5.5814(2) c = 7.8719(3) β = 89.920(4) V = 244.69(2)	6.03, 4.57, 1.33	0.92	$La_2Ti_2O_7$
	$La_2Ti_2O_7$	6(2)	$Pna2_1$	a = 25.730(6) b = 7.816(1) c = 5.552(1) V = 1116.4(4)		1.58	
0.5	$La_2Mg_{0.5}Zn_{0.5}TiO_6$	95(3)	$P2_1/n$	a = 5.5712(2) b = 5.5889(2) c = 7.8789(3) β = 89.961(3) V = 245.32(2)	5.99, 4.64, 1.31	0.96	$La_2Ti_2O_7$
	$La_2Ti_2O_7$	5(3)	$Pna2_1$	a = 25.742(8) b = 7.818(2) c = 5.543(2) V = 1115.6(5)		1.72	
0.75	$La_2Mg_{0.25}Zn_{0.75}TiO_6$	97(2)	$P2_1/n$	a = 5.5739(2) b = 5.5960(2) c = 7.8854(2) β = 89.937(3) V = 245.96(1)	6.84, 5.11, 1.40	1.20	$La_2Ti_2O_7$
	$La_2Ti_2O_7$	3(2)	$Pna2_1$	a = 25.732(8) b = 7.815(2) c = 5.542(2) V = 1115.2(9)		1.66	
1	La_2ZnTiO_6	95.8(20)	$P2_1/n$	a = 5.5760(2) b = 5.6066(1) c = 7.8918(2) β = 90.049(3) V = 246.71(1)	5.79, 4.50, 1.28	0.97	$La_2Ti_2O_7$ ZnO
	$La_2Ti_2O_7$	3(2)	$Pna2_1$	a = 25.72(1) b = 7.813(3) c = 5.543(2) V = 1113.9(8)		1.60	
	ZnO	1.2(1)	$P6_3mc$	a = 3.2497(5) c = 5.206(1) V = 47.61(2)		0.72	

In order to depict the crystal structure transformation process of $LM_{(1-w)}Z_wT$:0.005Bi^{3+}, 0.002Mn^{4+} with increasing *w* values, the schematic structure variation based on the refinement results is shown in Figure 3. It could be observed that LMT:0.005Bi^{3+}, 0.002Mn^{4+} and LZT:0.005Bi^{3+}, 0.002Mn^{4+} are isomorphic, which both belong to double perovskite-type ABB'O_6 family. The basically three-dimensional framework of $LM_{(1-w)}Z_wT$:0.005Bi^{3+}, 0.002Mn^{4+} ($0 \le w \le 1$) is built by vertex-sharing [Ti/Mg/ZnO_6] octahedra. Notably, the local symmetry and coordination environment between LMT:0.005Bi^{3+}, 0.002Mn^{4+} and LZT:0.005Bi^{3+}, 0.002Mn^{4+} are quite different. LMT:Bi^{3+}, Mn^{4+} belongs to orthorhombic (space group *Pbnm*) with unit-cell parameters a = 5.5546(2) Å, b = 5.5592(1) Å, c = 7.8652(2) Å and V = 242.87(1) $Å^3$, in which exists only one type Mg^{2+}/Ti^{4+} sites at *4b* (0.5, 0, 0) sites, forming [Mg/TiO_6] octahedra. La^{3+} ions are coordinated by twelve adjacent O^{2-} ions forming [LaO_{12}] polyhedron with high '*m*' (C_s) symmetry. While LZT:0.005Bi^{3+}, 0.002Mn^{4+} is indexed with a monoclinic unit cell (space group $P2_1/n$) with unit-cell parameters a = 5.5760(2) Å, b = 5.6066(1) Å, c = 7.8918 Å and V = 246.71(1) $Å^3$. There exists two different Zn^{2+}/Ti^{4+} sites, including Zn1/Ti1 (mainly occupied by Zn^{2+}) at *2c* (0, 0.5, 0) sites and Zn2/Ti2 (mainly occupied by Ti^{4+}) at *2d* (0, 0, 0.5) sites. In this case, La^{3+} is also coordinated by twelve adjacent O^{2-} ions forming [LaO_{12}] polyhedron with the lowest '*1*' (C_1) symmetry. In view of the appearance of phase transition from *Pbnm* to $P2_1/n$ in $LM_{(1-w)}Z_wT$:0.005Bi^{3+},0.002Mn^{4+} ($0 \le w \le 1$) phosphors, two obvious local structure variation could be observed. On the one hand, (Ti/Mg/Zn) site splits into two lattice sites, marked as (Ti1/Mg1/Zn1) and (Ti2/Mg2/Zn2) sites, which may exert influence on the luminescence of Mn^{4+}. On the other hand, the local symmetry of [LaO_{12}] polyhedron decrease from the '*m*' (C_s) symmetry to the lowest '*1*' (C_1) symmetry. The variation of local coordination environment of (Ti/Mg/Zn) site and symmetry of [LaO_{12}] polyhedron is suggested to influence the luminescence of Bi^{3+} and Mn^{4+} in $LM_{(1-w)}Z_wT$:0.005Bi^{3+}, 0.002Mn^{4+} ($0 \le w \le 1$) phosphors.

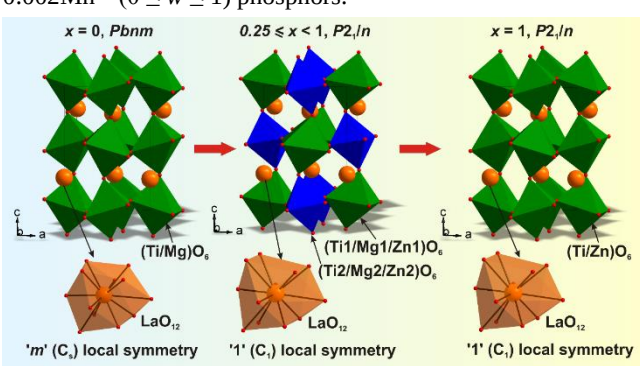

Figure 3. The crystal structure transformation process of $LM_{(1-w)}Z_wT$:0.005Bi^{3+}, 0.002Mn^{4+} ($0 \le w \le 1$) by phase transition. The main feature is one (Ti/Mg/Zn) site splitting into two (Ti1/Mg1/Zn1), (Ti2/Mg2/Zn2) sites, and the decreasing local symmetry of [LaO_{12}] polyhedron.

Figure 4a displays the SEM image of the representative $LM_{0.5}Z_{0.5}T$:0.005Bi^{3+}, 0.002Mn^{4+} sample. It can be observed that the as-prepared sample is assembled by irregular particles of about 0.2–0.5 μm in diameter. The elemental analysis is revealed via the SEM mapping images of $LM_{0.5}Z_{0.5}T$:0.005Bi^{3+}, 0.002Mn^{4+} in Figure 4b-4h. Evidently, the studied sample contains La, Mg, Zn, Ti, O, Bi and Mn elements, and they uniformly distribute throughout the whole viewing area. In addition, the peaks of La, Mg, Zn, Ti, O, Bi and Mn elements appear in EDS spectrum (Figure 4i), indicating that Bi^{3+} ions and Mn^{4+} ions are successfully doped into the $LM_{0.5}Z_{0.5}T$ solid solution. On the basis of the EDS result, the atomic ratio of La, Mg, Zn, Ti, O is calculated to be 3.94:1.06:1:1.93:13.72, which is very close to the theoretical atomic ratio in $LM_{0.5}Z_{0.5}T$:0.005Bi^{3+}, 0.002Mn^{4+}. These results demonstrate that the successful synthesis of the designed $LM_{(1-w)}Z_wT$:0.005Bi^{3+}, 0.002Mn^{4+} ($0 \le w \le 1$) samples. Moreover, the HRTEM images of representative LMT:0.005Bi^{3+}, 0.002Mn^{4+} and LZT:0.005Bi^{3+}, 0.002Mn^{4+} samples present clear lattice fringes (Figure 4j-4k), demonstrating good crystallinity. The d-spacings of LMT:0.005Bi^{3+}, 0.002Mn^{4+} is 2.7869 Å, corresponding to (202) plane, and LZT:0.005Bi^{3+}, 0.002Mn^{4+} is 2.6462 Å, corresponding to (204) plane, respectively.

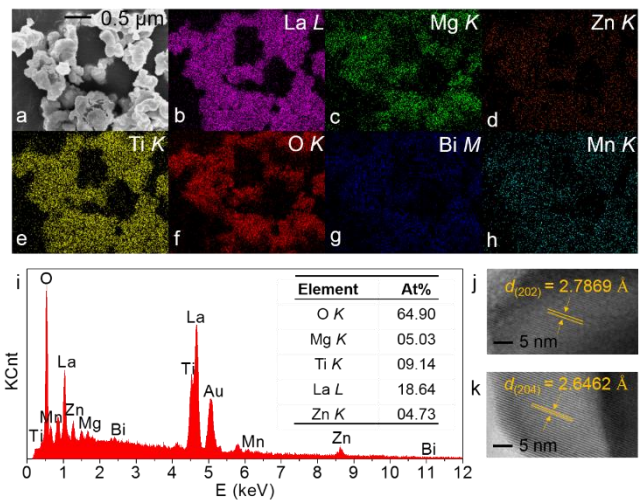

Figure 4. (a) SEM image of the representative $LM_{0.5}Z_{0.5}T$:0.005Bi^{3+}, 0.002Mn^{4+} sample. (b-h) The corresponding elemental mapping analysis for La, Mg, Zn, Ti, O, Bi and Mn elements in LM0.5Z0.5T:0.005Bi^{3+}, 0.002Mn^{4+}. (i) Energy-dispersive spectrum (EDS) of $LM_{0.5}Z_{0.5}T$:0.005Bi^{3+}, 0.002Mn^{4+}, and the inset is the atom percentage in $LM_{0.5}Z_{0.5}T$:0.005Bi^{3+}, 0.002Mn^{4+}. (j) HRTEM images of LMT:0.005Bi^{3+}, 0.002Mn^{4+} and LZT:0.005Bi^{3+}, 0.002Mn^{4+}.

Given the sensitivity of Bi^{3+} ions to the coordination environment, the optical properties of $LM_{(1-w)}Z_wT$:0.005Bi^{3+}, 0.002Mn^{4+} ($0 \le w \le 1$) samples with varying *w* values are discussed in details. The optical band gaps of LMT and LZT hosts are firstly calculated by following formula based on the diffuse reflection spectra:[36-38]

$$[F(R)h\nu]^{1/2} = A\,(h\nu - E_g)$$
$$F(R) = (1-R)^2/2R \qquad (1)$$

Where A stands for absorption constant, E_g represents the optical band gap, $h\nu$ is the photon energy, F(R) is the absorption coefficient, and R is the reflectance (%) coefficient, respectively. Figure 5a depicts plots of $[F(R)h\nu]^{1/2}$ versus $h\nu$ of LMT and LZT host. The calculated E_g values for LMT and LZT host are 3.95 eV and 3.84 eV respectively, indicating that both of LMT and LZT are suitable host for Bi^{3+} and Mn^{4+}-doping. To detect the photoluminescence absorption properties of Bi^{3+}, Mn^{4+} co-doped $LM_{(1-w)}Z_wT$ phosphors, the UV-vis diffusion reflection spectra (DRS) for different Zn^{2+} concentra-

tion samples (w = 0, 0.5, 1) are collected in Figure 5b, which mainly includes four absorption bands. The first absorption band located at about 330 nm should be ascribed to Mn-O charge transfer band (CTB). The second absorption band arises from $^1S_0 \rightarrow {}^1P_1/{}^3P_1$ transition of Bi^{3+} with the center at around 350 nm. The transitions of $^4A_2 \rightarrow {}^4T_1$ and $^4A_2 \rightarrow {}^2T_2$ of Mn^{4+} contribute to the third absorption band, which is from 355 nm to 475 nm. Finally, the forth absorption band from 450 nm to 600 nm with the maximum at around 500 nm originates from the $^4A_2 \rightarrow {}^4T_2$ transitions of Mn^{4+}.

To study the effect of phase transition and $Zn^{2+} \rightarrow Mg^{2+}$ substitution on the photoluminescence properties of $LM_{(1-w)}T_w$:0.005Bi^{3+}, 0.002Mn^{4+} ($0 \le w \le 1$), their photoluminescence excitation (PLE) and emission (PL) spectra are recorded and analyzed. Figure S4 (Supporting Information) and Figure 5c show the normalized PLE spectra of $LM_{(1-w)}T_w$:0.005Bi^{3+}, 0.002Mn^{4+} (w = 0-1) monitored at 420 nm for Bi^{3+} and 710 nm for Mn^{4+}, respectively. When monitored at 420 nm, the PLE spectra of Bi^{3+} possess absorption broad band from 275 nm to 375 nm with the maximum at 345 nm, attributed to $^1S_0 \rightarrow {}^1P_1/{}^3P_1$ transitions of Bi^{3+}. When monitored at 710 nm, all PLE spectra of w = 0-1.0 samples include two evidently broad absorption bands in the region of 275 nm-550 nm. The stronger absorption band is from 275 nm to 450 nm with the maximum at 340-395 nm, while the weak one is from 450 nm to 550 nm centered at 500 nm. Based on the Gaussian fitting function, the PLE spectra could be divided into four characteristic peaks, which originate from charge transfer band (CTB) of Mn-O and electron transition of $^4A_{2g} \rightarrow {}^4T_{1g}$, $^4A_{2g} \rightarrow {}^2T_{2g}$, $^4A_{2g} \rightarrow {}^4T_{2g}$ for Mn^{4+} (Figure S5a-5b). The Gaussian deconvoluted peaks of LMT:0.005Bi^{3+}, 0.002Mn^{4+} locate at 325 nm, 357 nm, 388 nm and 484 nm, respectively. For LZT:0.005Bi^{3+}, 0.002Mn^{4+}, its Gaussian deconvoluted peaks are 338 nm, 386 nm, 478 nm and 520 nm. These results are consistent with the above diffusion reflection spectra.

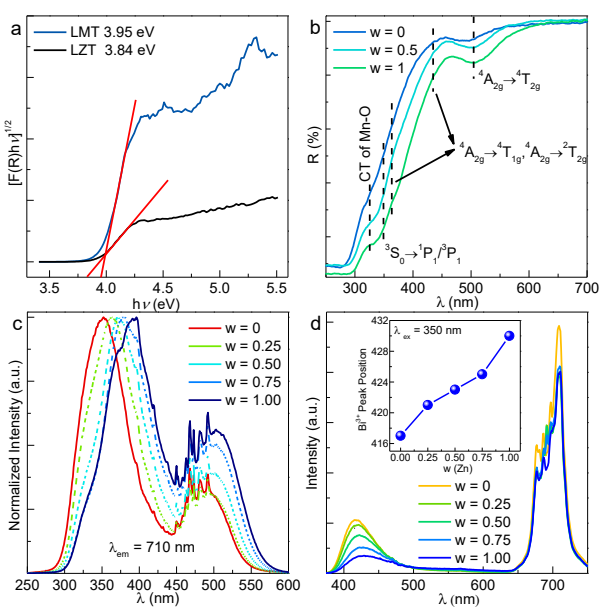

Figure 5. (a) The relationship of $[F(R)h\nu]^{1/2}$ vs photon energy $h\nu$ in LMT host and LZT host. (b) Diffuse reflectance spectra corresponding to $LM_{(1-w)}Z_wT$:0.005Bi^{3+}, 0.002Mn^{4+}(w = 0, 0.5, 1). (c) Normalized photoluminescence excitation (PLE) spectra of $LM_{(1-w)}Z_wT$;0.005Bi^{3+}, 0.002Mn^{4+} (w = 0, 0.25, 0.50, 0.75, 1). (d) Photoluminescence emission spectra of $LM_{(1-w)}Z_wT$:0.005Bi^{3+}, 0.002Mn^{4+} (w = 0, 0.25, 0.50, 0.75, 1), inset is the Bi^{3+} peak position as a function of Zn^{2+} concentration.

Obviously, a red shift appears in Mn^{4+} PLE spectra as w value increases. We speculate the variation of [Ti/Mg/ZnO_6] octahedra coordination environment is the primary reason. Owing to the special $3d^3$ electron configuration, the electron transition of Mn^{4+} energy levels is easily influenced by crystal filed (CF) environment. When $w \ge 0.25$, there exists phase transition in $LM_{(1-w)}Z_wT$:0.005Bi^{3+}, 0.002Mn^{4+} ($0 \le w \le 1$), causing by Zn/Mg/Ti splitting into two different sites. Thereafter, the CF symmetry of [Ti/Mg/ZnO_6] octahedra decreases, which is influenced by larger distortion with increasing Zn^{2+} concentration (Figure S6). As CF environment varying, Mn^{4+} excited state levels $^4T_{1g}$, $^2T_{2g}$ and $^4T_{2g}$ change accordingly,[39] resulting in PLE spectra red shift of Mn^{4+} ions in $LM_{(1-w)}Z_wT$:0.005Bi^{3+}, 0.002Mn^{4+} ($0 \le w \le 1$).

Upon exciting at 345 nm n-UV light, the PL spectra of $LM_{(1-w)}Z_wT$:0.005Bi^{3+}, 0.002Mn^{4+} samples simultaneously present the characteristic emission of Bi^{3+} and Mn^{4+} ions with the emission peaks at 420 nm and 710 nm, respectively, as shown in Figure 5d. According to above discussion, the larger Zn^{2+} ions occupy Zn/Mg/Ti sites, the average bond length of Zn/Mg/Ti-O gradually elongate (Figure S3), resulting in the expansion of [Zn/Mg/TiO_6] octahedra. Consequently, [LaO_{12}] polyhedra will be squeezed by adjacent [Zn/Mg/TiO_6] octahedra, which leads to the decreasing symmetry of [LaO_{12}] polyhedron from the 'm'(C_s) symmetry to the '1'(C_1) symmetry with increasing w (Figure 3). Finally, it generates red-shift in PL spectra of Bi^{3+} from 417 nm to 428 nm (inset of Figure 5d). However, CF strength seldomly influence the excited state level ^2E_g of Mn^{4+}.[40] Hence, red emission peaks of Mn^{4+} ions ($^2E_g \rightarrow {}^4A_{2g}$ transitions) basically locate at 710 nm with increasing Zn^{2+} concentration.

Energy Transfer from Bi^{3+} to Mn^{4+}

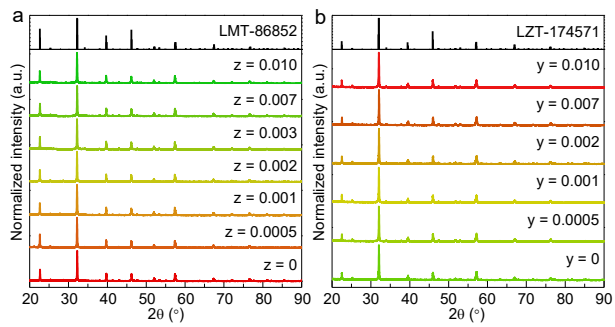

Figure 6. XRD patterns of (a) $LMT_{(1-z)}$:0.005Bi^{3+}, $z$$Mn^{4+}$ ($0 \le z \le 0.01$) samples and (b) $LZT_{(1-y)}$:0.005Bi^{3+}, $y$$Mn^{4+}$ ($0 \le y \le 0.01$) samples. The standard XRD data of LMT (ICSD No. 86852) and LZT (ICSD No. 174571) are shown as references.

Efficient energy transfer not only could extremely improve luminescence efficiency of activators but also could realize a controllable luminescence tuning of the characteristic emission from sensitizers to activators.[41] These changes could help optimize various luminescence performances of phosphors to promote their application in pc-WLEDs. According to the above structure discussion, Bi^{3+} and Mn^{4+} ions are suggested to preferentially occupy La^{3+} and Ti^{4+} sites in LMT and LZT systems, respectively. However, a small quantity of Mn^{4+} ions possibly enter into Mg^{2+} or Zn^{2+} sites, due to the same site-occupation of Mg^{2+}/Zn^{2+} and Ti^{4+} (Table S1, w =0 and w = 1).

In order to enhance the red emission of Mn^{4+} ions, we design the $Bi^{3+}\rightarrow Mn^{4+}$ energy transfer in LMT and LZT series. A series of Bi^{3+}-doped, Mn^{4+}-doped and Bi^{3+}/Mn^{4+} co-doped LMT and LZT phosphors are successfully synthesized. Figure S7 (Supporting Information) and Figure 6 exhibit the XRD of the as-prepared powders, all the XRD diffraction peaks of as-prepared samples are in good agreement with standard LMT (ICSD No. 86852) and LZT (ICSD No. 174571), respectively, without apparent impurities. These results prove that all as-prepared samples are pure phases.

Table 2. CIE color coordinates of $LMT_{(1-z)}$:0.005Bi^{3+}, zMn^{4+} ($0 \le z \le 0.01$) and $LZT_{(1-y)}$:0.005Bi^{3+}, yMn^{4+} ($0 \le y \le 0.01$)

sample	z/yMn^{4+}	x	y
	$LMT_{(1-z)}$:0.005Bi^{3+}, zMn^{4+} ($0 \le z \le 0.01$)		
1	0	0.1729	0.0689
2	0.0005	0.1974	0.0884
3	0.001	0.2211	0.1061
4	0.002	0.2581	0.1255
5	0.003	0.2765	0.1487
6	0.007	0.3124	0.1747
7	0.010	0.3202	0.2086
	$LZT_{(1-y)}$:0.005Bi^{3+}, yMn^{4+} ($0 \le y \le 0.01$)		
1	0	0.2142	0.1716
2	0.0005	0.2793	0.2238
3	0.001	0.2851	0.2089
4	0.002	0.3979	0.2436
5	0.007	0.4064	0.2389
6	0.010	0.4117	0.2465

Figure 7a shows PLE and PL spectra of LMT:0.005Bi^{3+} and LMT:0.002Mn^{4+}, meanwhile the PLE and PL spectra of $L_{(1-u)}MT$:uBi^{3+} ($0 \le u \le 0.03$) and $LMT_{(1-z)}$:zMn^{4+} ($0 \le z \le 0.01$) are shown in Figure S8-S9 (Supporting Information), respectively. For LMT:0.005Bi^{3+}, there is an obvious absorption band from 275 nm to 375 nm centered at 340 nm, which is ascribed to the $^1S_0\rightarrow{}^1P_1$ and $^1S_0\rightarrow{}^3P_1$ transitions of Bi^{3+}. When monitoring at 340 nm, blue emission (375-500 nm) with the maximum at 417 nm of Bi^{3+} is detected, originating from the $^3P_1\rightarrow{}^1S_0$ transitions. When Mn^{4+} ions enter into LMT host, a strong red emission band from 650 nm to 750 nm with the emission peak at 710 nm is observed due to Mn^{4+}: ^2E_g-$^4A_{2g}$ transitions. Apparently, there is spectral overlap from 455 nm to 490 nm between the emission spectrum of Bi^{3+} and the excitation spectra of Mn^{4+}. Simultaneously, a co-excitation band from 300 nm to 375 nm exists in LMT:0.005Bi^{3+} and LMT:0.002Mn^{4+} samples. Hence, there is a great possibility to expect energy transfer between Bi^{3+} and Mn^{4+} in LMT. To verify the $Bi^{3+}\rightarrow Mn^{4+}$ energy transfer in LMT host, a range of PL spectra of the $LMT_{(1-z)}$:0.005Bi^{3+}, zMn^{4+} ($0 \le z \le 0.01$) samples under 340 nm wavelength are collected in Figure 7b. It is found that both blue emission from Bi^{3+} and red emission from Mn^{4+} appear in all of Bi^{3+}/Mn^{4+} co-doped samples. When mixing the Bi^{3+}-doping concentration in $LMT_{(1-z)}$:0.005Bi^{3+}, zMn^{4+} system, the emission intensity of Bi^{3+} gradually decreases with the increase of Mn^{4+}-doping concentration. While the emission intensity of Mn^{4+} presents a monotonous increase before z = 0.002, as shown in the inset of Figure 7b. These results also indicate that there is an energy transfer in LMT: Bi^{3+}/Mn^{4+} co-doped phosphors. Beyond z = 0.002, concentration quenching happens to Mn^{4+} emission. It is because that the distance of adjacent Mn^{4+} becomes shorter with increasing its doping concentration, and then the Mn^{4+}-Mn^{4+} interaction strengthens, resulting in the luminescence quenching of Mn^{4+} in LMT: Bi^{3+}/Mn^{4+} co-doped system.

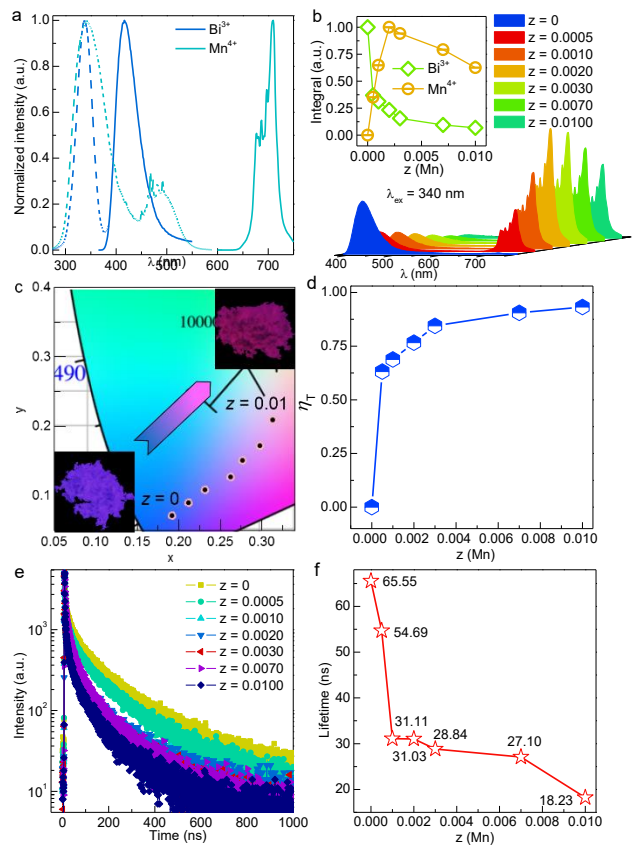

Figure 7. (a) The PLE and PL spectra of LMT:0.005Bi^{3+} (blue) and LMT:0.002Mn^{4+} (cyan). (b) The PL spectra of $LMT_{(1-z)}$:0.005Bi^{3+}, zMn^{4+} ($0 \le z \le 0.01$). The inset is integrated intensity of Bi^{3+} and Mn^{4+} emission as a function of Mn^{4+} concentrations (z). (c) The CIE chromaticity coordinates diagram for $LMT_{(1-z)}$:0.005Bi^{3+}, zMn^{4+} ($0 \le z \le 0.01$), and the insets are luminescence photographs of LMT:0.005Bi^{3+} and LMT:0.005Bi^{3+}, 0.010Mn^{4+}, respectively, under 365 nm n-UV excitation. (d) The energy transfer efficiency (η_T) of $LMT_{(1-z)}$:0.005Bi^{3+}, zMn^{4+} ($0 \le z \le 0.01$) as a function of Mn^{4+} concentrations (z). (e) Photoluminescence decay curves of Bi^{3+} emission detected at 370 nm for $LMT_{(1-z)}$:0.005Bi^{3+}, zMn^{4+} ($0 \le z \le 0.01$). (f) The decay lifetime of $LMT_{(1-z)}$:0.005Bi^{3+}, zMn^{4+} ($0 \le z \le 0.01$) as a function of Mn^{4+} concentrations (z).

Figure 7c and Table 2 show the CIE chromaticity coordinates of $LMT_{(1-z)}$:0.005Bi^{3+}, zMn^{4+} ($0 \le z \le 0.01$) vary from (0.1729, 0.0689) to (0.3202, 0.2086) with z values increasing, and thus the emission colors could be adjusted from blue to pink region. The corresponding luminescence photos of z = 0 and z = 0.01 samples also demonstrate the color tuning from blue to pink light, further confirming the existence of $Bi^{3+}\rightarrow Mn^{4+}$ energy transfer. The energy transfer efficiency of $LMT_{(1-z)}$:0.005Bi^{3+}, zMn^{4+} ($0 \le z \le 0.01$) could be determined by the following equation:[42]

$$\eta_T = 1 - \frac{I_S}{I_{S0}} \quad (2)$$

η_T stands for the energy transfer efficiency, I_S and I_{S0} represent emission intensity with and without Mn^{4+} ions respectively. The calculated η_T of $LMT_{(1-z)}$:0.005Bi^{3+}, zMn^{4+} ($0 \le z \le 0.01$) are shown in Figure 7d, which are 63.15%, 68.81%, 76.64%, 84.48%, 90.54% and 93.24% for z = 0.0005, 0.001, 0.002, 0.003, 0.007 and 0.010, respectively. This result proves the highly efficient of $Bi^{3+}\rightarrow Mn^{4+}$ energy transfer in $LMT_{(1-z)}$:0.005Bi^{3+}, zMn^{4+} ($0 \le z \le 0.01$) phosphors.

To better understand luminescence dynamics during the energy transfer of $LMT_{(1-z)}$:0.005Bi^{3+}, zMn^{4+} ($0 \le z \le 0.01$). The photoluminescence decay curves and calculated lifetime values of Bi^{3+} for various Mn^{4+} concentrations are measured and depicted in Figure 7e and 7f, respectively. Under 370 nm n-UV light exciting, the decay lifetime for Bi^{3+} emission of $LMT_{(1-z)}$:0.005Bi^{3+}, zMn^{4+} ($0 \le z \le 0.01$) samples are determined through the following equation:

$$I_T = I_0 \exp(\frac{-t}{\tau}) \quad (3)$$

Where I_0 and I_t represent luminescence intensities of Bi^{3+} at t_0 and t; τ stands for luminescence decay lifetimes for corresponding samples. With the increase of Mn^{4+} concentration, the decay lifetimes are calculated to be 65.55, 54.69, 31.11, 31.03, 28.84, 27.10, and 18.23 ns, respectively. Obviously, the lifetimes of Bi^{3+} present a monotonous decrease with increasing z values, which is a very favorable evidence to confirm the existence of $Bi^{3+}\rightarrow Mn^{4+}$ energy transfer.

Normally, energy transfer process mainly originates from two kinds of interaction: One is exchange interaction and the other is multipolar interaction, which are determined based on the critical distance (R_c). R_c is the distance between sensitizers and activators. It is known that if the distance between sensitizers and activators is shorter than 4 Å, it happens exchange interaction; If it locates between 4 Å and 27 Å, it happens multipolar interaction. The R_c is usually judged by following equation:[43-44]

$$R_c \approx 2(\frac{3V}{4\pi x_c N})^{1/3} \quad (4)$$

Where V is the volume of the unit cell, x_c is the sum concentration of Bi^{3+} ions and Mn^{4+} ions, N is the number of cations in the unit cell. In the $LMT_{(1-z)}$:0.005Bi^{3+}, zMn^{4+} ($0 \le z \le 0.01$) series, V is 242.87 $Å^3$, x_c is 0.007, and N is 4, respectively. Consequently, the calculated R_c is 25.49 Å. When energy transfer occurs from Bi^{3+} ions to Mn^{4+} ions in LMT host, the multipolar interaction plays a major role.

Since the crystal structure similarity between LMT and LZT, the $Bi^{3+}\rightarrow Mn^{4+}$ energy transfer also could be expected in LZT host. Figure 8a collects the PLE and PL spectra of LZT:0.005Bi^{3+} and LZT:0.002Mn^{4+}. When Bi^{3+} ions incorporate into LZT host, it also shows a broad absorption from 275 nm to 375 nm centered at 355 nm due to the $^1S_0\rightarrow{}^1P_1/{}^3P_1$ transitions of Bi^{3+}. Under 355 nm wavelength exciting, the emission spectra of LZT:0.005Bi^{3+} include two evident emission bands from 375 nm to 650 nm with two emission centers at 428 nm and 550 nm, respectively. This phenomenon exists throughout the whole $L_{(1-x)}ZT$:xBi^{3+} series (Figure S10). Nevertheless, on the basis of the previous Rietveld refinement result in Table S1 (w = 1), there is only one site for La^{3+} ions in LZT. Hence, we speculate that a small number of Bi^{3+} ions possibly occupy interstitial lattice position of LZT, generating the 550 nm emission. When Mn^{4+} ions enter into LZT host (Figure S11), its PLE and PL spectra are almost same as that of LMT:Mn^{4+}. Notably, wide spectra overlap between the emission spectra of Bi^{3+} and the excitation spectra of Mn^{4+} is observed in Figure 8a. It indicates that the energy transfer may happen between Bi^{3+} ions and Mn^{4+} ions in $LZT_{(1-y)}$:0.005Bi^{3+}, yMn^{4+} ($0 \le y \le 0.01$). When fixing the Bi^{3+} concentrations and changing the Mn^{4+}-doping concentrations, it is found that Bi^{3+} blue emission of gradually decrease while Mn^{4+} red emission simultaneously increases before y = 0.002 in Bi^{3+}/Mn^{4+} co-doped LZT samples (Figure 8b and 8d). The reduced emission intensity for Mn^{4+} ions beyond y = 0.002 should be also attributed to concentration quenching effect. Meanwhile, the CIE chromaticity diagram in Figure 8c reveals that the color coordinates of $LZT_{(1-y)}$:0.005Bi^{3+}, yMn^{4+} ($0 \le y \le 0.01$) gradually shift from (0.2142, 0.1716) to (0.4117, 0.2465) with increasing Mn^{4+} concentrations, implying a broad color tuning from blue to red light. The detailed CIE color coordinates values of $LZT_{(1-y)}$:0.005Bi^{3+}, yMn^{4+} ($0 \le y \le 0.01$) samples calculated via its PL spectra are summarized in Table 2. The above results further confirm the appearance of $Bi^{3+}\rightarrow Mn^{4+}$ energy transfer in LZT host. The $Bi^{3+}\rightarrow Mn^{4+}$ energy transfer efficiency in $LZT_{(1-y)}$: 0.005Bi^{3+}, yMn^{4+} ($0 \le y \le 0.01$) are similarly calculated by the formula 1 (Figure 8e). The η_T values of $LZT_{(1-y)}$: 0.005Bi^{3+}, yMn^{4+} ($0 \le y \le 0.01$) are 20.29%, 32.94%, 76.18%, 89.31%, 91.59% for y = 0.0005, 0.001, 0.002 0.007, 0.01, respectively, revealing the effective energy transfer in $LZT_{(1-y)}$:0.005Bi^{3+}, yMn^{4+}. In addition, the R_c between Bi^{3+} and Mn^{4+} in the $LZT_{(1-y)}$: 0.005Bi^{3+}, yMn^{4+} ($0 \le y \le 0.01$) is calculated to be 25.28 Å, which is also ascribed to electric multipolar interaction.

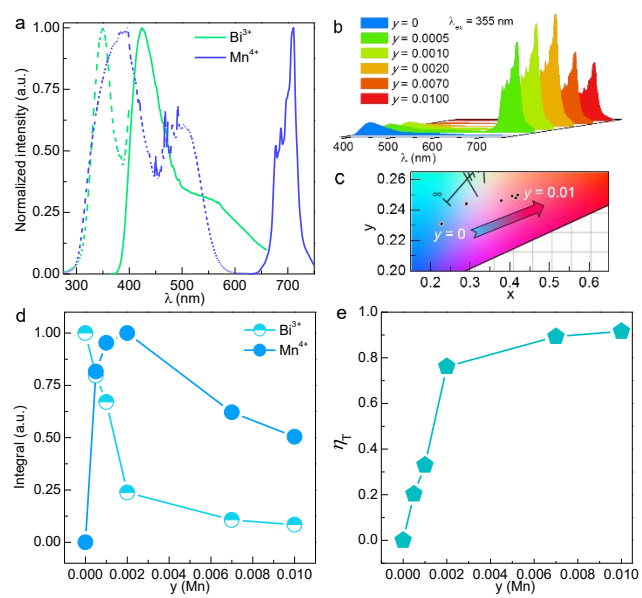

Figure 8. (a) The PLE and PL spectra of LZT:0.005Bi^{3+} (green) and LZT:0.002Mn^{4+} (navy blue). (b) The PL spectra and (c) CIE chromaticity coordinates diagram for $LZT_{(1-y)}$:0.005Bi^{3+}, yMn^{4+} ($0 \le y \le 0.01$). (d) Integrated intensity of Bi^{3+} and Mn^{4+} emission as a function of Mn^{4+}-doping concentrations (y). (e) The energy transfer efficiency of $LZT_{(1-y)}$:0.005Bi^{3+}, yMn^{4+} ($0 \le y \le 0.01$) as a function of Mn^{4+}-doping concentrations (y).

The specific type of electric multipolar interaction between Bi^{3+} and Mn^{4+} in $LAT_{(1-y)}$:0.005Bi^{3+}, $y$$Mn^{4+}$ (A = Mg, Zn) ($0 \leq y \leq 0.01$) systems can be obtained from Dexter's formula:[45-47]

$$\frac{\eta_{s0}}{\eta_s} \propto C^{n/3} \tag{5}$$

Where η_{S0}/η_S stands for the ratio of quantum efficiency without and with Bi^{3+}-doped samples. C represents the total concentration of Bi^{3+} and Mn^{4+} ions. n is a constant which influences the interaction relationship of Bi^{3+} and Mn^{4+}, when n = 6, 8, and 10, matching with dipole–dipole, dipole–quadrupole and quadrupole–quadrupole interactions, respectively. The value of η_{S0}/η_S could be approximately replaced by the ratio of emission intensity of I_{S0}/I_S. Hence, the following formula can be expressed as follow:

$$\frac{I_{s0}}{I_s} \propto C^{n/3} \tag{6}$$

where I_{S0} represents initial emission intensity of Bi^{3+}, and I_S represents emission intensity Bi^{3+} of Bi^{3+}/Mn^{4+} co-doped phosphors. When n = 6, 8, 10, the relation between I_{S0}/I_S and $C^{n/3}$ of $LMT_{(1-z)}$: 0.005Bi^{3+}, $z$$Mn^{4+}$ ($0 \leq z \leq 0.01$) and $LZT_{(1-y)}$: 0.005Bi^{3+}, $y$$Mn^{4+}$ ($0 \leq y \leq 0.01$) are showed in Figure 9a-9c and 9d-9f, respectively. The maximal correlation coefficient of linear fitting can be achieved at n = 6 both for the above two series, indicating that the dipole-dipole interaction contributes to the energy transfer between Bi^{3+} and Mn^{4+} $LAT_{(1-y)}$:0.005Bi^{3+}, $y$$Mn^{4+}$ (A = Mg, Zn) ($0 \leq y \leq 0.01$) samples.

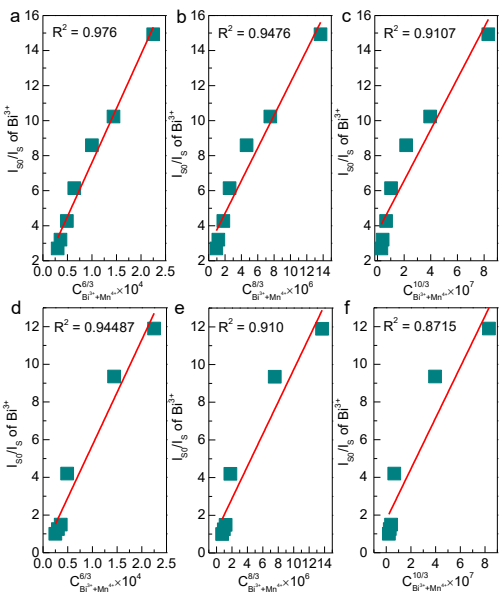

Figure 9. Dependence of I_{S0}/I_S of Bi^{3+} ions on (a) $C_{(Bi^{3+}+Mn^{4+})}^{6/3}$,(b) $C_{(Bi^{3+}+Mn^{4+})}^{8/3}$ and (c) $C_{(Bi^{3+}+Mn^{4+})}^{10/3}$ for $LMT_{(1-z)}$:0.005Bi^{3+}, $z$$Mn^{4+}$ ($0 \leq z \leq 0.01$), dependence of I_{S0}/I_S of Bi^{3+} ions on (d) $C_{(Bi^{3+}+Mn^{4+})}^{6/3}$, (e) $C_{(Bi^{3+}+Mn^{4+})}^{8/3}$ and (f) $C_{(Bi^{3+}+Mn^{4+})}^{10/3}$ for $LZT_{(1-y)}$:0.005Bi^{3+}, $y$$Mn^{4+}$ ($0 \leq y \leq 0.01$).

According to the previous experiment results and analysis, a schematic energy level diagram for the electronic transitions and the energy transfer process in Bi^{3+}/Mn^{4+} co-doped $LAT_{(1-y)}$:0.005Bi^{3+}, $y$$Mn^{4+}$ (A = Mg, Zn) ($0 \leq y \leq 0.01$) phosphors are depicted in Figure 10. Upon exciting with 340 or 355 nm n-UV light, the electrons in Bi^{3+} ions are excited from the ground state $^1S_0$ to the excited state $^3P_1$, $^3P_2$, $^1P_1$. Then, a part of electrons occur relaxation from $^3P_2$ and $^1P_1$ energy level to $^3P_1$ energy level and return to ground state $^1S_0$ energy level, generating a blue emission (417 nm or 428 nm). Meanwhile, other electron located at excited state level $^3P_1$ transfers their energy to the excited state $^4T_{2g}$ energy level of neighboring Mn^{4+} ions. In addition, Mn^{4+} ions can also be excited from $^4A_{2g}$ to $^4T_{2g}$, $^2T_{2g}$, $^4T_{1g}$ energy levels. After the excited electrons in Mn^{4+} ions occur relaxation to ^2E_g energy level and then return to $^4A_{2g}$ energy level, accompanying a far-red light emission centered at 710 nm. Through designing the energy transfer from Bi^{3+} to Mn^{4+}, the far-red emission efficiency of Mn^{4+} ions in LMT and LZT systems could be markedly improved. The internal quantum efficiency values (IQEs) increase from 31.5% (LMT:0.002Mn^{4+}) to 59.5% (LMT:0.005Bi^{3+}, 0.002Mn^{4+}) and from 40.3% (LZT:0.002Mn^{4+}) to 70.8% (LZT:0.005Bi^{3+}, 0.002Mn^{4+}) in LMT and LZT systems, respectively.

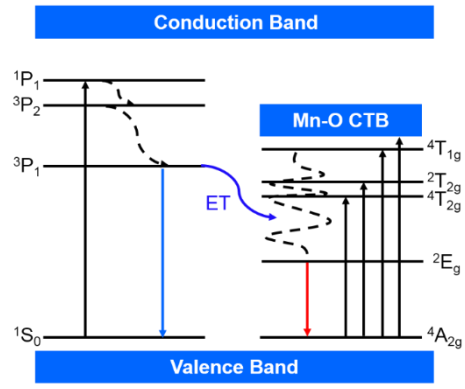

Figure 10. A schematic energy level diagram for the electronic transitions and the energy transfer process in $LAT_{(1-y)}$:0.005Bi^{3+}, $y$$Mn^{4+}$ (A = Mg, Zn) ($0 \leq y \leq 0.01$) systems.

Thermal Stability

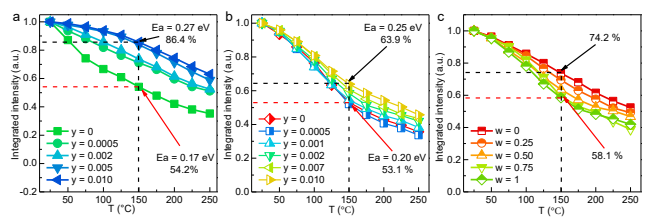

Figure 11. Temperature-dependent integrated emission spectra of (a) $LMT_{(1-z)}$:0.005Bi^{3+}, $z$$Mn^{4+}$ ($0 \leq z \leq 0.01$), (b) $LZT_{(1-y)}$:0.005Bi^{3+}, $y$$Mn^{4+}$ ($0 \leq y \leq 0.01$) and (c) $LM_{(1-w)}Z_wT$:0.005Bi^{3+}, 0.002Mn^{4+} ($0 \leq w \leq 1$) excited under 350 nm n-UV light.

In practice, the working temperature of pc-WLEDs can reach 150°C, which will greatly influence the emission intensity, luminescence lifetime and chromaticity of phosphors.[48-50] Hence, thermal stability is a very important index for phosphors to evaluate its practical application in pc-WLEDs lighting area. In this regard, the thermal stability of $LMT_{(1-z)}$:0.005Bi^{3+}, $z$$Mn^{4+}$ ($0 \leq z \leq 0.01$), $LZT_{(1-y)}$:0.005Bi^{3+}, $y$$Mn^{4+}$ ($0 \leq y \leq 0.01$) and $LM_{(1-w)}Z_wT$:0.005Bi^{3+}, 0.002Mn^{4+} ($0 \leq w \leq 0.01$) are detected from 25 °C to 250 °C by temperature-dependent PL spectra (Figure 11). The PL intensity of all studied samples gradually decreases with increasing temperature, which should be attributed to the thermal quenching effect induced by non-radiation transition process. However, as increasing Mn^{4+} and Mg^{2+}-doped concentration, the corresponding emission intensities are all enhanced. As for $LMT_{(1-}$

$_{z)}$:0.005Bi^{3+}, zMn^{4+} ($0 \le z \le 0.01$), LZT$_{(1-y)}$:0.005Bi^{3+}, yMn^{4+} ($0 \le y \le 0.01$) phosphors, at 150°C, when Mn^{4+} concentration varies from 0 to 0.01, the emission intensity at 150°C of LMT$_{(1-z)}$:0.005Bi^{3+}, zMn^{4+} ($0 \le z \le 0.01$) increases from 0.54 to 0.86 of initial intensity at 25°C; for LZT$_{(1-y)}$:0.005Bi^{3+}, yMn^{4+} ($0 \le y \le 0.01$), the emission intensity at 150°C increase from 0.53 to 0.64 of initial intensity at 25°C. The increase of temperature-dependent PL intensity may be related to non-radiative transition process, which can be represent by thermal activation energy ΔE_a. The ΔE_a can be obtained as following formula:

$$I(T) = \frac{I_0}{1 + C\exp(-\Delta E_a / kT)} \quad (7)$$

I_0 is integrated emission intensity at 25°C and $I(T)$ is integrated emission intensity at temperature T. k is the Boltzmann constant ($k = 8.62 \times 10^{-5}$ eV). ΔE_a is thermal activation energy. Then, ΔE_a can be calculated by plotting $\ln[(I_0/I_T)-1]$ against $10000/T$. The calculated ΔE_a values of LMT$_{(1-z)}$:0.005Bi^{3+}, zMn^{4+} and LZT$_{(1-y)}$:0.005Bi^{3+}, yMn^{4+} all gradually enhance with increasing Mn^{4+} concentration (Figure 11a-11b). In regard to LM$_{(1-w)}$Z$_w$T:0.005Bi^{3+}, 0.002Mn^{4+} ($0 \le w \le 1$) phosphors, the temperature-dependent PL intensity at 150°C increases from 0.58 (w = 1) to 0.78 (w = 0) with increasing Mg^{2+} concentrations. Based on the former discussion, decreasing distorts of [Zn/Mg/TiO$_6$] octahedra (Figure S5) will result in the higher local symmetry for Mn^{4+}-doping. Hence, the more Mg^{2+} ions are doped in LM$_{(1-w)}$Z$_w$T:0.005Bi^{3+}, 0.002Mn^{4+} ($0 \le w \le 1$) phosphors, the more stable structure is, which contributes to the enhancement of thermal stability for Mn^{4+} ions red emission (Figure 11c). These results demonstrate that the non-radiative transition is weakened with the increase of Mn^{4+} and Mg^{2+} concentration, accordingly improving the thermal stability.

WLEDs Application

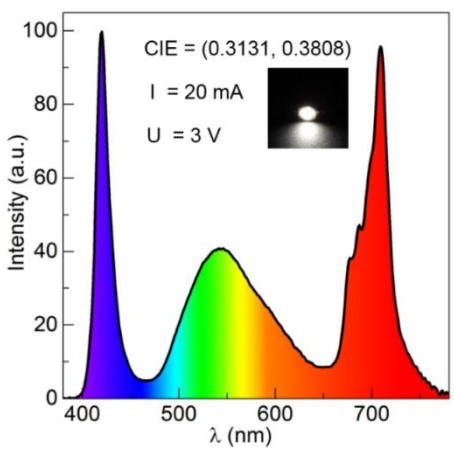

Figure 12. Electroluminescence spectrum and luminescence photograph of pc-WLEDs device fabricated by commercially available green Ba$_3$Si$_6$O$_{12}$N$_2$:Eu^{2+} phosphor and the representative red LZT:0.005Bi^{3+}, 0.002Mn^{4+} phosphor driven by n-UV LED chip (λ = 420 nm).

To estimate the practical application of as-prepared phosphor on pc-WLEDs devices, we fabricated the pc-WLEDs device by combining n-UV LED chip (λ = 420 nm) and the mixture of commercially available green Ba$_3$Si$_6$O$_{12}$N$_2$:Eu^{2+} phosphor and the representative red LZT:0.005Bi^{3+}, 0.002Mn^{4+} phosphor. The performance of fabricated pc-WLEDs and luminescence photograph are show in Figure 12. Under a voltage of 3.15 V and current of 20 mA, the obtained pc-WLEDs device exhibits white emission with low corresponding color temperature (CCT = 5825 K) and high CIR (R_a = 87.5), of which the CIE coordinates locate at (0.3131, 0.3808). These results indicate that the as-prepared Bi^{3+}/Mn^{4+} co-doped LAT (A = Mg, Zn) double-perovskite phosphor could be an excellent red-emitting phosphor candidate for application in warm pc-WLEDs.

■ CONCLUSIONS

In this work, we successfully synthesized a series of L$_{(1-u)}$MT:uBi^{3+}, LMT$_{(1-z)}$:zMn^{4+}, LMT$_{(1-z)}$:0.005Bi^{3+} zMn^{4+}, L$_{(1-x)}$ZT:xBi^{3+}, LZT$_{(1-y)}$:yMn^{4+}, LZT$_{(1-y)}$:0.005Bi^{3+}, yMn^{4+} and LM$_{(1-w)}$Z$_w$T:0.005Bi^{3+}, 0.002Mn^{4+} phosphors by high-temperature solid-state reaction in air. The Rietveld refinement clearly reveal that there exists a phase transition from orthorhombic cell (*Pbnm*) to monoclinic cell ($P2_1/n$) among the La(Mg$_{1-w}$Zn$_w$)TiO$_6$: Bi^{3+}, Mn^{4+} solid solution when doping Zn^{2+} ions into the LaMgTiO$_6$. This phase transition makes (Ti/Mg/Zn) sites splitting into two (Ti1/Mg1/Zn1), (Ti2/Mg2/Zn2) sites, decreasing local structure of [LaO$_{12}$] polyhedron from the '*m*'(C_s) symmetry to the lowest symmetry '*1*' (C_1) and increasing crystal field distortion of [Ti/Mg/ZnO$_6$] octahedra. Along with this phase transition, the PLE spectra of Mn^{4+} and PL spectra of Bi^{3+} present gradual red shift. In addition, the energy transfers from Bi^{3+} and Mn^{4+} are successfully designed by occupying La and Ti/Mg/Zn sites, respectively. The corresponding energy transfer efficiency are 93.24% for LMT$_{(1-z)}$:0.005Bi^{3+} zMn^{4+} and 91.59% for LZT$_{(1-y)}$:0.005Bi^{3+}, yMn^{4+}. Moreover, the IQYs values increase from 31.5% (LMT:0.002Mn^{4+}) to 59.5% (LMT:0.005Bi^{3+}, 0.002Mn^{4+}) and from 40.3% (LZT:0.002Mn^{4+}) 70.8% (LZT:0.005Bi^{3+}, 0.002Mn^{4+}) for LMT and LZT systems, respectively. Bi^{3+}→Mn^{4+} energy transfer mechanisms in the studied systems are determined to be dipole-dipole interaction. Moreover, the doping of Mg^{2+} and Mn^{4+} ions can also help to enhance the thermal stabilities of phosphors by lattice modification and energy transfer. At 150 °C, the temperature-dependent PL intensity increase from 0.54 of initial intensity to 0.86, 0.53 of initial intensity to 0.64 and 0.58 of initial intensity to 0.78 for LMT$_{(1-z)}$:0.005Bi^{3+}, zMn^{4+}, LZT$_{(1-y)}$:0.005Bi^{3+}, yMn^{4+} and LM$_{(1-w)}$Z$_w$T:0.005Bi^{3+}, 0.002Mn^{4+} respectively, which are attributed to the decrease of non-radiative transition by increasing Mn^{4+} and Mg^{2+} concentration. The performance of the fabricated pc-WLEDs devices indicates that LZT:0.005Bi^{3+}, 0.01Mn^{4+} could be a promising red phosphor for pc-WLEDs. This work offers an efficient strategy for designing Bi^{3+}→Mn^{4+} energy transfer in double perovskite-type structure to improve the red emission of Mn^{4+} ions and realizing controllable color tuning for generating novel phosphors for pc-WLEDs application.

■ ASSOCIATED CONTENT

Supporting Information. This material is available free of charge via the Internet at http://pubs.acs.org."
Synchrotron XRD pattern, PL spectra, diffuse reflectance spectra, CIE coordination diagram, crystallographic lattice parameters and bond length information including in Figure S1-S11 and Table S1-S2.

■ AUTHOR INFORMATION

Corresponding Author

*E-mail: ggli@cug.edu.cn
*E-mail: jlin@ciac.ac.cn

ORCID

Jun Lin: 0000-0001-9572-2134

Notes

The authors declare no competing financial interest.

ACKNOWLEDGMENT

This work was supported by the National Natural Science Foundation of China (Grant Nos. 51672259, 51672265, 21521092, 51750110511), Engineering Research Center of Nano-Geomaterials of Ministry of Education, China University of Geosciences (Wuhan) (No. NGM2016KF002), the Key Research Program of Frontier Sciences, CAS (Grant No. YZDY-SSW-JSC018), and projects for science and technology development plan of Jilin province (20170414003GH), the Program for Jiangmen Innovative Research Team (No.[2017]385)，major program of basic research and applied research of Guangdong Province (2017KZDXM083).

■ REFERENCES

(1) Qin, X.; Liu, X.; Huang, W.; Bettinelli, M.; Liu, X. Lanthanide-activated phosphors based on 4*f*-5*d* optical transitions: Theoretical and experimental aspects. *Chem. Rev.* **2017**, *117*, 4488–4527.

(2) George, N. C.; Denault, K. A.; Seshadri, R. Phosphors for solid-state white lighting. *Annu. Rev. Mater. Res.* **2013**, *43*, 481–501.

(3) Li, G.; Tian, Y.; Zhao, Y.; Lin, J. Recent progress in luminescence tuning of Ce^{3+} and Eu^{2+}-activated phosphors for pc-WLEDs. *Chem. Soc. Rev.* **2015**, *44*, 8688–8713.

(4) Wang, L.; Xie, R. J.; Suehiro, T.; Takeda, T.; Hirosaki, N. Down-conversion nitride materials for solid state lighting: Recent advances and perspectives. *Chem. Rev.* **2018**, *118*, 1951–2009.

(5) Xia, Z.; Liu, Q. Progress in discovery and structural design of color conversion phosphors for LEDs. *Prog. Mater. Sci.* **2016**, *84*, 59–117.

(6) Lin, C. C.; Liu, R. S. Advances in phosphors for light-emitting diodes. *J. Phys. Chem. Lett.* **2011**, *2*, 1268–1277.

(7) Ueda, J.; Dorenbos, P.; Bos, A. J. J.; Meijerink, A.; Tanabe, S., Insight into the thermal quenching mechanism for $Y_3Al_5O_{12}:Ce^{3+}$ through thermoluminescence excitation Spectroscopy. *J. Phys. Chem. C* **2015**, *119*, 25003–25008.

(8) George, N. C.; Pell, A. J.; Dantelle, G.; Page, K.; Llobet, A.; Balasubramanian, M.; Pintacuda, G.; Chmelka, B. F.; Seshadri, R. Local environments of dilute activator ions in the solid-state lighting phosphor $Y_{3-x}Ce_xAl_5O_{12}$. *Chem. Mater.* **2013**, *25*, 3979–3995.

(9) Zhong, J.; Zhao, W.; Zhuang, W.; Xiao, W.; Zheng, Y.; Du, F.; Wang, L. Origin of spectral blue shift of Lu^{3+}-codoped YAG:Ce^{3+} phosphor: First-principles study. *ACS Omega* **2017**, *2*, 5935–5941.

(10) Qiao, J.; Ning, L.; Molokeev, M. S.; Chuang, Y. C.; Liu, Q.; Xia, Z. Eu^{2+} site preferences in the mixed cation $K_2BaCa(PO_4)_2$ and thermally stable luminescence. *J. Am. Chem. Soc.* **2018**, *140*, 9730–9736.

(11) Zhao, M.; Liao, H.; Ning, L.; Zhang, Q.; Liu, Q.; Xia, Z. Next-generation narrow-band green-emitting $RbLi(Li_3SiO_4)_2:Eu^{2+}$ phosphor for backlight display application. *Adv. Mater.* **2018**, 1802489.

(12) Wang, C. Y.; Takeda, T.; Ten Kate, O. M.; Tansho, M.; Deguchi, K.; Takahashi, K.; Xie, R. J.; Shimizu, T.; Hirosaki, N. Ce-doped $La_3Si_{6.5}Al_{1.5}N_{9.5}O_{5.5}$, a rare highly efficient blue-emitting phosphor at short wavelength toward high color rendering white LED application. *ACS Appl. Mater. Interfaces* **2017**, *9*, 22665–22675.

(13) Xie, R. J.; Hirosaki, N.; Suehiro, T.; Xu, F. F.; Mitomo, M. A simple, efficient synthetic route to $Sr_2Si_5N_8:Eu^{2+}$-based red phosphors for white light-emitting diodes. *Chem. Mater.* **2006**, *18*, 5578–5583.

(14) Sakuma, K. White light-emitting diode lamps using oxynitride and nitride phosphor materials. *IEICE T. Electron.* **2005**, *E88-C*, 2057–2064.

(15) Deng, B.; Liu, S.; Zhou, C. S.; Liu, H.; Chen, J.; Yu, R. Eu^{3+}-activated $Gd_8V_2O_{17}$: Energy transfer, Luminescence, and temperature-dependence characteristics. *Chem. Eur. J.* **2018**, *24*, 11627–11636.

(16) Du, P.; Huang, X.; Yu, J. S. Facile synthesis of bifunctional Eu^{3+}-activated $NaBiF_4$ red-emitting nanoparticles for simultaneous white light-emitting diodes and field emission displays. *Chem. Eng. J.* **2018**, *337*, 91–100.

(17) Han, J.; Li, L.; Peng, M.; Huang, B.; Pan, F.; Kang, F.; Li, L.; Wang, J.; Lei, B. Toward Bi^{3+} Red luminescence with no visible reabsorption through manageable energy interaction and crystal defect modulation in single Bi^{3+}-doped $ZnWO_4$ crystal. *Chem. Mater.* **2017**, *29*, 8412–8424.

(18) Fang, M. H.; Wu, W. L.; Jin, Y.; Lesniewski, T.; Mahlik, S.; Grinberg, M.; Brik, M. G.; Srivastava, A. M.; Chiang, C. Y.; Zhou, W.; Jeong, D.; Kim, S. H.; Leniec, G.; Kaczmarek, S. M.; Sheu, H. S.; Liu, R. S. Control of luminescence by tuning of crystal symmetry and local structure in Mn^{4+} -activated narrow band fluoride phosphors. *Angew. Chem. Int. Ed.* **2018**, *57*, 1797–1801.

(19) Han, J.; Pan, F.; Molokeev, M. S.; Dai, J.; Peng, M.; Zhou, W.; Wang, J. Redefinition of crystal structure and $Bi^{(3+)}$ yellow luminescence with strong near-Ultraviolet excitation in $La_3BWO_9:Bi^{(3+)}$ phosphor for white light-emitting diodes. *ACS Appl. Mater. Interfaces* **2018**, *10*, 13660–13668.

(20) Zhu, Y.; Qiu, Z.; Ai, B.; Lin, Y.; Zhou, W.; Zhang, J.; Yu, L.; Mi, Q.; Lian, S. Significant improved quantum yields of $CaAl_{12}O_{19}:Mn^{4+}$ red phosphor by co-doping Bi^{3+} and B^{3+} ions and dual applications for plant cultivations. *J. Lumine.* **2018**, *201*, 314–320.

(21) Zhou, Z.; Zhong, Y.; Xia, M.; Zhou, N.; Lei, B.; Wang, J.; Wu, F. Tunable dual emission of $Ca_3Al_4ZnO_{10}:Bi^{3+}$, Mn^{4+} via energy transfer for indoor plant growth lighting. *J. Mater. Chem. C* **2018**, *6*, 8914–8922.

(22) Dang, P.; Liang, S.; Li, G.; Wei, Y.; Cheng, Z.; Lian, H.; Shang, M.; Al Kheraif, A. A.; Lin, J. Full color luminescence tuning in Bi^{3+}/Eu^{3+}-doped $LiCa_3MgV_3O_{12}$ garnet phosphors based on local lattice distortion and multiple energy transfers. *Inorg. Chem.* **2018**, *57*, 9251–9259.

(23) Zhu, H.; Lin, C. C.; Luo, W.; Shu, S.; Liu, Z.; Liu, Y.; Kong, J.; Ma, E.; Cao, Y.; Liu, R. S.; Chen, X. Highly efficient non-rare-earth red emitting phosphor for warm white light-emitting diodes. *Nat. Commun.* **2014**, *5*, 4312.

(24) Huang, L.; Liu, Y.; Yu, J.; Zhu, Y.; Pan, F.; Xuan, T.; Brik, M. G.; Wang, C.; Wang, J. Highly stable K2SiF6:Mn^{4+}@K2SiF6 composite phosphor with narrow red emission for white LEDs. *ACS Appl. Mater. Interfaces* **2018**, *10*, 18082–18092.

(25) Li, L.; Pan, Y.; Chen, Z.; Huang, S.; Wu, M. Tunable luminescence and energy transfer properties of Bi^{3+} and Mn^{4+} co-doped $Ca_{14}Al_{10}Zn_6O_{35}$ phosphors for agricultural applications. *RSC Adv.* **2017**, *7*, 14868–14875.

(26) Fuh, H. R.; Liu, Y. P.; Xiao, Z. R.; Wang, Y. K. New type of ferromagnetic insulator: Double perovskite La_2NiMO_6 (M = Mn, Tc, Re, Ti, Zr, and Hf). *J. Magn. Magn. Mater.* **2014**, *357*, 7–12.

(27) Zhong, J.; Chen, D.; Chen, X.; Wang, K.; Li, X.; Zhu, Y.; Ji, Z. Efficient rare-earth free red-emitting $Ca_2YSbO_6:Mn^{4+}$, M (M = Li^+, Na^+, K^+, Mg^{2+}) phosphors for white light-emitting diodes. *Dalton Trans.* **2018**, *47*, 6528–6537.

(28) Zhong, J.; Zhou, S.; Chen, D.; Li, J.; Zhu, Y.; Li, X.; Chen, L.; Ji, Z. Enhanced luminescence of a $Ba_2GdSbO_6:Mn^{4+}$ red phosphor via cation doping for warm white light-emitting diodes. *Dalton Trans.* **2018**, *47*, 8248–8256.

(29) Li, K.; Lian, H.; Van Deun, R. A novel deep red-emitting phosphor $KMgLaTeO_6:Mn^{4+}$ with high thermal stability and quantum yield for w-LEDs: structure, site occupancy and photoluminescence properties. *Dalton Trans.* **2018**, *47*, 2501–2505.

(30) Sun, Q.; Wang, S.; Devakumar, B.; Li, B.; Sun, L.; Liang, J.; Huang, X. Synthesis and photoluminescence properties of novel far-red-emitting $BaLaMgNbO_6:Mn^{4+}$ phosphors for plant growth LEDs. *RSC Adv.* **2018**, *8*, 28538–28545.

(31) Zhong, J.; Chen, D.; Yuan, S.; Liu, M.; Yuan, Y.; Zhu, Y.; Li, X.; Ji, Z. Tunable optical properties and enhanced thermal quenching of non-rare-earth double-perovskite $(Ba_{1-x}Sr_x)_2YSbO_6:Mn^{4+}$ red phosphors based on composition modulation. *Inorg. Chem.* **2018**, *57*, 8978–8987.

(32) Takeda, Y.; Kato, H.; Kobayashi, M.; Kobayashi, H.; Kakihana, M. Photoluminescence properties of Mn^{4+}-activated perovskite-type titanates, $La_2MTiO_6:Mn^{4+}$ (M = Mg and Zn). *Chem. Lett.* **2015**, *44*, 1541–1543.

(33) Meden, A.; Čeh, M., Structure determination and Rietveld refinement of $La(Mg_{0.5}Ti_{0.5})O_3$. *Mater. Sci. Forum*. **1998**, *278–281*, 773–778.

(34) Vigen, C. K.; Bjørheim, T. S.; Haugsrud, R. The role of B-site cations on proton conductivity in double perovskite oxides La_2MgTiO_6 and La_2MgZrO_6. *Int. J. Hydrogen Energ.* **2012**, *37*, 7983–7994.

(35) Aguadero, A.; Alonso, J. A.; Martínez-Lope, M. J.; Fernández-Díaz, M. T. Crystallo-chemical evolution of the La_2ZnTiO_6 double perovskite upon reduction: A structural study. *Solid State Sci.* **2011**, *13*, 13–18.

(36) Wang, X.; Zhao, Z.; Wu, Q.; Li, Y.; Wang, Y., A garnet-based $Ca_2YZr_2Al_3O_{12}:Eu^{3+}$ red-emitting phosphor for n-UV light emitting diodes and field emission displays: Electronic structure and luminescence properties. *Inorg. Chem.* **2016**, *55*, 11072–11077.

(37) Liu, Y.; Silver, J.; Xie, R. J.; Zhang, J.; Xu, H.; Shao, H.; Jiang, J.; Jiang, H., An excellent cyan-emitting orthosilicate phosphor for NUV-pumped white LED application. *J. Mater. Chem. C* **2017**, *5,* 12365–12377.

(38) Wei, Y.; Cao, L.; Lv, L.; Li, G.; Hao, J.; Gao, J.; Su, C.; Lin, C. C.; Jang, H. S.; Dang, P.; Lin, J. Highly efficient blue emission and superior thermal stability of $BaAl_{12}O_{19}:Eu^{2+}$ phosphors based on highly symmetric crystal structure. *Chem. Mater.* **2018**, *30*, 2389–2399.

(39) Wu, W. L.; Fang, M. H.; Zhou, W.; Lesniewski, T.; Mahlik, S.; Grinberg, M.; Brik, M. G.; Sheu, H. S.; Cheng, B. M.; Wang, J.; Liu, R. S. High color rendering index of $Rb_2GeF_6:Mn^{4+}$ for light-emitting diodes. *Chem. Mater.* **2017**, *29*, 935–939.

(40) Adachi, S. Photoluminescence properties of Mn^{4+} -activated oxide phosphors for use in white-LED applications: A review. *J. Lumine.* **2018**, *202*, 263–281.

(41) Zhang, Z.; Ma, C.; Gautier, R.; Molokeev, M. S.; Liu, Q.; Xia, Z. Structural confinement toward giant enhancement of red emission in Mn^{2+} -based phosphors. *Adv. Funct. Mater.* **2018**, 1804150.

(42) Fang, Y. C.; Huang, X. R.; Juang, Y. D.; Chu, S. Y.; Ballato, J. Color-tunable blue to green $Ca_{4-1.5x}Ta_2O_9$: xTb^{3+} phosphor: Cross-relaxation mechanism and thermal stability. *J. Am. Ceram. Soc.* **2012**, *95*, 1613–1618.

(43) Xiao, W.; Zhang, X.; Hao, Z.; Pan, G. H.; Luo, Y.; Zhang, L.; Zhang, J., Blue-emitting $K_2Al_2B_2O_7:Eu^{2+}$ phosphor with high thermal stability and high color purity for near-UV-pumped white light-emitting diodes. *Inorg. Chem.* **2015**, *54*, 3189–3195.

(44) Wang, Z.; Ye, W.; Chu, I. H.; Ong, S. P. Elucidating structure–composition–property relationships of the β-SiAlON:Eu^{2+} phosphor. *Chem.Mater*. **2016**, *28*, 8622–8630.

(45) Zhang, M.; Liang, Y.; Tang, R.; Yu, D.; Tong, M.; Wang, Q.; Zhu, Y.; Wu, X.; Li, G. Highly efficient $Sr_3Y_2(Si_3O_9)_2:Ce^{3+},Tb^{3+}/Mn^{2+}/Eu^{2+}$ phosphors for white LEDs: structure refinement, color tuning and energy transfer. *RSC Adv.* **2014**, *4*, 40626–40637.

(46) Li, G.; Wang, Y.; Zeng, W.; Chen, W.; Han, S.; Guo, H.; Li, Y. Photo-/cathodoluminescence and energy transfer properties of novel Ce^{3+} singly doped and Ce^{3+}/Tb^{3+} codoped $NaBaScSi_2O_7$ phosphors. *J. Mater. Chem. C* **2016**, *4*, 3304–3312.

(47) Li, G.; Hou, Z.; Peng, C.; Wang, W.; Cheng, Z.; Li, C.; Lian, H.; Lin, J., Electrospinning derived one-dimensional LaOCl: Ln^{3+} (Ln = Eu/Sm, Tb, Tm) nanofibers, nanotubes and microbelts with multicolor-tunable emission properties. *Adv. Funct. Mater.* **2010**, *20*, 3446–3456.

(48) Kim, Y. H.; Arunkumar, P.; Kim, B. Y.; Unithrattil, S.; Kim, E.; Moon, S. H.; Hyun, J. Y.; Kim, K. H.; Lee, D.; Lee, J. S.; Im, W. B. A zero-thermal-quenching phosphor. *Nat. Mater.* **2017**, *16*, 543–550.

(49) Strobel, P.; Maak, C.; Weiler, V.; Schmidt, P. J.; Schnick, W. Ultra-narrow-band blue-emitting oxoberyllates $AELi_2[Be_4O_6]:Eu^{2+}$ (AE = Sr, Ba) paving the way to efficient RGB pc-LEDs. *Angew. Chem. Int. Ed.* **2018**, *57*, 8739–8743.

(50) Sharma, S. K.; Lin, Y. C.; Carrasco, I.; Tingberg, T.; Bettinelli, M.; Karlsson, M. Weak thermal quenching of the luminescence in the $Ca_3Sc_2Si_3O_{12}:Ce^{3+}$ garnet phosphor. *J. Mater. Chem. C* **2018**, *6*, 8923–8933.

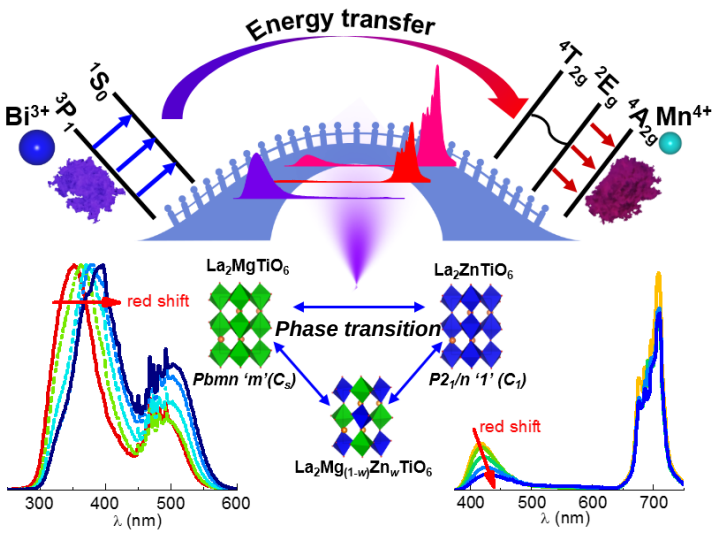

Enhanced red emission and photoluminescence tuning by Bi^{3+}→Mn^{4+} energy transfer and symmetric changes in Bi^{3+}/Mn^{4+}-doped La_2ATiO_6 (A = Mg, Zn) double perovskite structure phosphors.